Hindawi
Mathematical Problems in Engineering
Volume 2021, Article ID 8950945, 13 pages
https://doi.org/10.1155/2021/8950945

Research Article

Meshing Stiffness Parametric Vibration of Coaxial Contrarotating Encased Differential Gear Train

Donglin Zhang[1] **Rupeng Zhu**[1] **Miaomiao Li**[1] **Wuzhong Tan**[2] **and Pingjun Li**[2]

[1]*National Key Laboratory of Science and Technology on Helicopter Transmission, Nanjing University of Aeronautics and Astronautics, Nanjing 210016, China*
[2]*AECC Hunan Aviation Powerplant Research Institute, Zhuzhou 412002, China*

Correspondence should be addressed to Rupeng Zhu; rpzhu_nuaa@163.com

Received 1 August 2020; Revised 1 February 2021; Accepted 8 February 2021; Published 26 February 2021

Academic Editor: Adrian Neagu

Planetary gears are widely used in mechanical transmission systems, but the vibration and noise affect their reliability and life. In this paper, the torsional dynamic model of an encased differential planetary gear with coaxial contrarotating outputs considering the time-varying meshing stiffness, damping, and phase difference of all gear pairs is established. By solving the equations of the derived system, three types of natural frequencies with different multiplicities of the system are obtained. The multiscale method is used to study the parametric vibration stability caused by the time-varying meshing stiffness, and the results are verified by numerical simulation. The dynamic characteristics of elastic meshing force are analyzed from time domain and frequency domain. The variation of the dynamic load factor of each gear pair with input speed and the relationship between its peak position and the natural frequency of the derived system are discussed. The results show that there is an unequal coupling phenomenon of meshing frequency between the meshing forces of different planetary sets. In the absence of external excitation, the meshing stiffness parameters not only excite the main resonance response of the system but also cause superharmonic resonance, subharmonic resonance, and combined resonance.

1. Introduction

Due to the existence of an encased structure, the coaxial contrarotating encased differential gear train can transmit torque through multiple paths, so it has stronger load-carrying capacity, more compact structure, and wider transmission ratio range than the ordinary multistage planetary gear train. It is widely used in the fields of helicopter transmission, marine power, and aeroengine. However, it is difficult to design the parameters of the system due to the requirement of constant speed reverse output of the internal and external output shafts, and the vibration and noise caused by internal excitations such as time-varying stiffness and errors also challenge its application. Howe and Mckibbin [1, 2] studied various gear drive system configurations that can realize the coaxial counterrotating of the fan rotors, and, on this basis, the lubrication and efficiency of differential gear train configuration are analyzed.

Parametric stability of gear systems caused by time-varying meshing stiffness has been extensively studied. Lin and Parker [3, 4] used multiscale method to study the effects of meshing stiffness parameters on the instability of the two-stage gear system and planetary gear system and derived a design expression for controlling the instability region by adjusting the stiffness parameters. Liu et al. [5] used the perturbation method to derive the expression of the system parameters instability with both meshing stiffness and bearing stiffness fluctuations, which is verified by Floquet theory. Qiu et al. [6, 7] established a lumped parameter model of a planetary gear considering time-varying meshing stiffness, damping, and input speed fluctuations and studied the effects of damping and input speed fluctuations on instability by the perturbation analysis and numerical method. Canchi and Parker [8] studied the parameter excitation of the rotating ring gear under time-varying stiffness and obtained the conditions of the ring-planet mesh phasing and contact ratio, which can suppress the parameter instability of the flexible ring gear in the planetary gear system. Based on the hybrid continuous discrete model, Parker [9, 10] obtained the parameter expression of the instability boundary of the planetary gear system with elastic continuous ring gear by using the structural modal characteristics and multiscale method.

Scholars have carried out many studies on the dynamic characteristics of meshing forces and multipath load distribution caused by time-varying meshing stiffness and error of planetary gear system. Inalpolat and Kahraman [11] established a nonlinear dynamic model including periodic time-varying mesh stiffnesses and gear tooth separation that can predict the sidebands of planetary gear set having manufacturing errors and rotating carrier and compared the predicted meshing force spectrum with the measured meshing force spectrum. Sondkar and Kahraman [12] used a three-dimensional dynamic model of the herringbone planetary gear train to analyze the variation of the maximum meshing force amplitude with the meshing frequency under different staggering phase angles of the left and right gears. Sun et al. [13] and Dong et al. [14] established the nonlinear dynamic model of planetary gear train and studied the influence of different load-sharing structures on the load-sharing performance.

At present, the research mainly focuses on single-stage or multistage planetary gear train, and the research on the dynamic coupling characteristics of the compound planetary gear train is not enough. In the coaxial contrarotating encased differential gear train, the inner and outer shafts are output in the opposite direction, and there are many output components that affect each other, so the dynamic coupling characteristics of the system are more complicated.

In this paper, a multi-degree-of-freedom torsional dynamics model considering the time-varying meshing stiffness and mesh phasing of the encased differential gear train, which is widely used in coaxial twin-rotor helicopters, is established. The multiscale method is used to analyze the vibration characteristics of the system caused by the fluctuation of meshing stiffness. The elastic meshing force is obtained by solving the differential equations using the Runge-Kutta method. The coupling characteristics of meshing frequency of different planetary set and the fluctuation characteristics of the dynamic load factor with the rotating speed are analyzed.

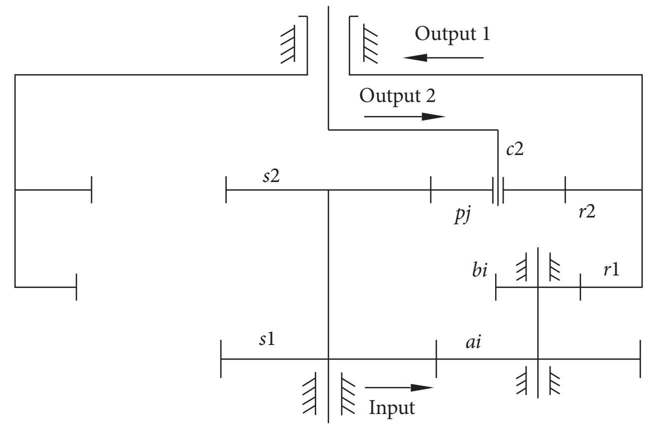

Figure 1: Schematic diagram of coaxial contrarotating encased differential gear train.

2. Dynamic Model of the Encased Differential Gear Train

Coaxial contrarotating encased differential gear train is shown in Figure 1. The encased stage consists of the sun gear $s1$, stepped planets ai and bi, and ring gear $r1$, and the differential stage consists of the sun gear $s2$, planets pj, and ring gear $r2$. The input power is transmitted to the ring gear and the carrier, respectively, through the encased stage and the differential stage to realize the reverse double output. By reasonable design of system parameters, the output speeds of ring gear $r2$ and carrier $c2$ can be equal [15].

Define the torsional deformation of each component of the gear system as generalized coordinates:

$$\mathbf{x} = \left[u_{s1}, u_{s2}, u_{r1}, u_{r2}, u_{c2}, u_{a1}, \ldots, u_{aM}, u_{b1}, \ldots, u_{bM}, u_{p1}, \ldots, u_{pN}\right]^T, \tag{1}$$

where M and N are the numbers of stepped planet gears and planet gears, respectively. For simplicity, the following assumptions are made: the planets of each planetary set are evenly arranged and have equal mass and moment of inertia. The torsional stiffness of each stepped planet is equal. The friction and error of the system are not considered.

The torsional dynamic model of the coaxial contrarotating gear system is shown in Figure 2. In the figure, k_s and k_x represent the torsional stiffness of the sun gear shaft and the stepped planet gear shaft, respectively, and k_r is the torsional stiffness between the rings $r1$ and $r2$. k_{s1ai}, k_{r1bi}, k_{s2pj}, and k_{r2pj} are the meshing stiffnesses between the sun $s1$ and the stepped planets ai, the ring $r1$ and the stepped planets bi, the sun $s2$ and the planets pj, and the ring $r2$ and the planets pj, respectively. Damping symbols are similar.

2.1. Stiffness. The Fourier series expression of the time-varying meshing stiffness considering the mesh phasing is [4]

$$k_m(t) = k_m^a + 2k_m^v \sum_{l=1}^{\infty} \left(a_m^{(l)} \cos l\omega_m t + b_m^{(l)} \sin l\omega_m t\right), \tag{2}$$

where

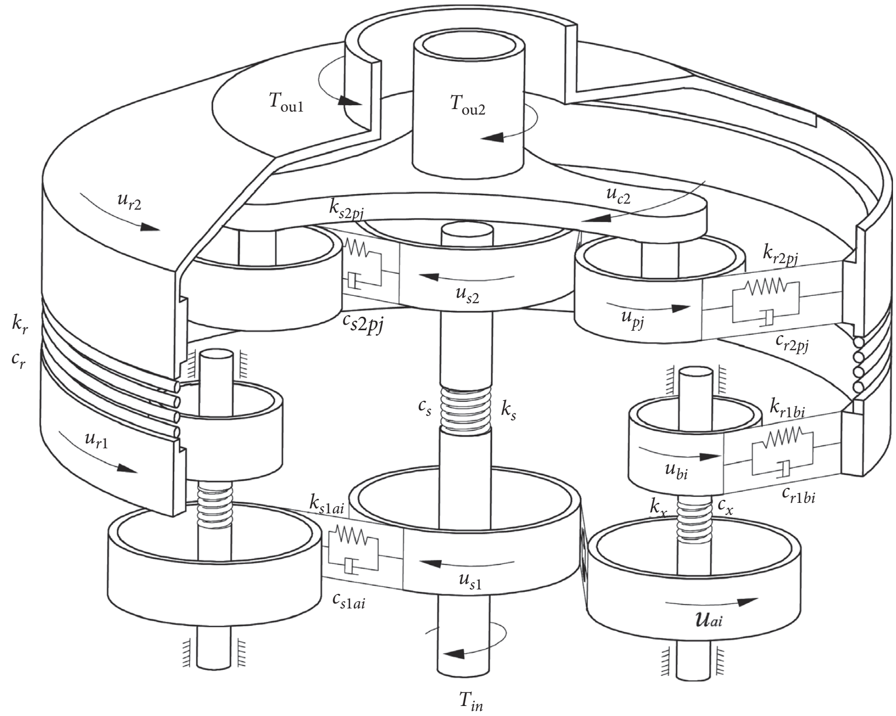

Figure 2: Torsional dynamic model for the coaxial contrarotating gear train.

$$a_m^{(l)} = \frac{2}{\pi l}\cos\left[\pi l\left(2\gamma_m + \varepsilon_m\right)\right]\sin\left(\pi l \varepsilon_m\right),$$
$$b_m^{(l)} = \frac{2}{\pi l}\sin\left[\pi l\left(2\gamma_m + \varepsilon_m\right)\right]\sin\left(\pi l \varepsilon_m\right). \quad (3)$$

In the formula, k_m^a and $2k_m^v$ are the mean component and fluctuation value of the mesh stiffness of the gear pair m, ω_m is the meshing frequency, ε_m is the contact ratio, and γ_m is the mesh phasing.

2.2. Damping. The meshing damping of gear pair m is [16]

$$c_m = 2\xi_m\sqrt{\frac{I_{m1}\cdot I_{m2}}{I_{m1}r_{m2}^2 + I_{m2}r_{m1}^2}k_m^a}. \quad (4)$$

In the formula, ξ_m is the meshing damping coefficient, I_{m1} and I_{m2} are the moments of inertia of the gears, and r_{m1} and r_{m2} are the base radii of the gears.

The torsional damping of the shaft z is

$$c_z = 2\xi_z\sqrt{k_z\frac{I_{z1}I_{z2}}{I_{z1} + I_{z2}}}, \quad (5)$$

where ξ_z is the relative torsional damping coefficient of the shaft z, k_z is the torsional stiffness, and I_{z1} and I_{z2} are the moments of inertia of the components connected to the shaft.

3. The Equations of Motion for the Gear Train

According to Newton's law, the equations of motion for the encased differential gear train are obtained as follows:

$$\frac{I_{s1}}{r_{bs1}^2}\ddot{u}_{s1} + \sum_{i=1}^{M}\left(k_{s1ai}\delta_{s1ai} + c_{s1ai}\dot{\delta}_{s1ai}\right) + \frac{k_s}{r_{bs1}}\left(\frac{u_{s1}}{r_{bs1}} - \frac{u_{s2}}{r_{bs2}}\right) + \frac{c_s}{r_{bs1}}\left(\frac{\dot{u}_{s1}}{r_{bs1}} - \frac{\dot{u}_{s2}}{r_{bs2}}\right) = \frac{T_{\text{in}}}{r_{bs1}}, \quad (6)$$

$$\frac{I_{s2}}{r_{bs2}^2}\ddot{u}_{s2} + \sum_{j=1}^{N}\left(k_{s2pj}\delta_{s2pj} + c_{s2pj}\dot{\delta}_{s2pj}\right) - \frac{k_s}{r_{bs2}}\left(\frac{u_{s1}}{r_{bs1}} - \frac{u_{s2}}{r_{bs2}}\right) + \frac{c_s}{r_{bs2}}\left(\frac{\dot{u}_{s1}}{r_{bs1}} - \frac{\dot{u}_{s2}}{r_{bs2}}\right) = 0, \quad (7)$$

$$\frac{I_{r1}}{r_{br1}^2}\ddot{u}_{r1} - \sum_{i=1}^{M}\left(k_{r1bi}\delta_{r1bi} + c_{r1bi}\dot{\delta}_{r1bi}\right) + \frac{k_r}{r_{br1}}\left(\frac{u_{r1}}{r_{br1}} - \frac{u_{r2}}{r_{br2}}\right) + \frac{c_r}{r_{br1}}\left(\frac{\dot{u}_{r1}}{r_{br1}} - \frac{\dot{u}_{r2}}{r_{br2}}\right) = 0, \quad (8)$$

$$\frac{I_{r2}}{r_{br2}^2}\ddot{u}_{r2}-\sum_{j=1}^{N}\left(k_{r2pj}\delta_{r2pj}+c_{r2pj}\dot{\delta}_{r2pj}\right)-\frac{k_r}{r_{br2}}\left(\frac{u_{r1}}{r_{br1}}-\frac{u_{r2}}{r_{br2}}\right)-\frac{c_r}{r_{br2}}\left(\frac{\dot{u}_{r1}}{r_{br1}}-\frac{\dot{u}_{r2}}{r_{br2}}\right)=-\frac{T_{ou1}}{r_{br2}}, \tag{9}$$

$$\left(\frac{I_{c2}+NI_p}{r_{c2}^2}+Nm_p\right)\ddot{u}_{c2}-\sum_{j=1}^{N}\left(k_{s2pj}\delta_{s2pj}+c_{s2pj}\dot{\delta}_{s2pj}\right)\cos\alpha_{s2}-\sum_{j=1}^{N}\left(k_{r2pj}\delta_{r2pj}+c_{r2pj}\dot{\delta}_{r2pj}\right)\cos\alpha_{r2}=-\frac{T_{ou2}}{r_{c2}}, \tag{10}$$

$$\frac{I_a}{r_{ba}^2}\ddot{u}_{ai}-k_{s1ai}\delta_{s1ai}-c_{s1ai}\dot{\delta}_{s1ai}+\frac{k_x}{r_{ba}}\left(\frac{u_{ai}}{r_{ba}}-\frac{u_{bi}}{r_{bb}}\right)+\frac{c_x}{r_{bm}}\left(\frac{\dot{u}_{ai}}{r_{ba}}-\frac{\dot{u}_{bi}}{r_{bb}}\right)=0, \tag{11}$$

$$\frac{I_b}{r_{bb}^2}\ddot{u}_{bi}-\frac{k_x}{r_{bb}}\left(\frac{u_{ai}}{r_{ba}}-\frac{u_{bi}}{r_{bb}}\right)-\frac{c_x}{r_{bb}}\left(\frac{\dot{u}_{ai}}{r_{ba}}-\frac{\dot{u}_{bi}}{r_{bb}}\right)+k_{r1bi}\delta_{r1bi}+c_{r1bi}\dot{\delta}_{r1bi}=0, \tag{12}$$

$$\frac{I_p}{r_{bp}^2}\ddot{u}_{pj}-k_{s2pj}\delta_{s2pj}-c_{s2pj}\dot{\delta}_{s2pj}+k_{r2pj}\delta_{r2pj}+c_{r2pj}\dot{\delta}_{r2pj}=0. \tag{13}$$

In the above equations, the relative displacement of gear mesh is

$$\begin{aligned}\delta_{s1ai}&=u_{s1}-u_{ai},\\ \delta_{s2pj}&=u_{s2}-u_{pj}-u_{c2}\cos\alpha'_{s2p},\\ \delta_{r1bi}&=u_{bi}-u_{r1},\\ \delta_{r2pj}&=u_{pj}-u_{r2}-u_{c2}\cos\alpha'_{r2p},\end{aligned} \tag{14}$$

where I_h ($h = s1, s2, r1, r2, c2, m, n, p$) are the moments of inertia of the component h, r_{bh} is the base circle radius of the gear h, r_{c2} is the distance from the center of planet to the center of the carrier, m_p is the mass of planet, $\alpha_{s2p}{}'$ and $\alpha_{r2p}{}'$ are the working pressure angles of the sun-planet and ring-planet mesh, T_{in} is the input torque, and T_{ou1} and T_{ou2} are the load torques applied to the carrier and ring gear, respectively.

Substituting equation (14) into (6)–(13), the matrix form of the system equations can be obtained as follows:

$$\mathbf{M}\ddot{\mathbf{x}}+\mathbf{C}\dot{\mathbf{x}}+\mathbf{K}\mathbf{x}=\mathbf{Q}, \tag{15}$$

where $\boldsymbol{M}$, $\boldsymbol{C}$,$\mathbf{K}$, and $\boldsymbol{Q}$ are generalized mass matrix, damping matrix, stiffness matrix, and external load array, respectively, as shown in Appendix A.

Disregarding damping and external forces, the equation for the free vibration of the system is

$$\mathbf{M}\ddot{\mathbf{x}}+(\mathbf{K}_a+\mathbf{K}_v)\mathbf{x}=\mathbf{0}. \tag{16}$$

In the equation, $\boldsymbol{K}_a$ is the mean stiffness matrix, including torsional stiffness and comprehensive meshing stiffness, and $\mathbf{K}_v$ is the variable stiffness matrix.

4. Dynamic Equations Decoupled and Stability Analysis

Let $\mathbf{K}_v$ in equation (16) be zero; then the derived system equation is

$$\mathbf{M}\ddot{\mathbf{x}}+\mathbf{K}_a\mathbf{x}=\mathbf{0}. \tag{17}$$

The eigensolutions can be obtained by solving formula (17).

$$\mathbf{K}_a\boldsymbol{\varphi}^{(i)}=\boldsymbol{\omega}_i^2\mathbf{M}\boldsymbol{\varphi}^{(i)}, \tag{18}$$

where $\boldsymbol{\varphi}^{(i)}$ are the vibration modes of the derived system and ω_i are natural frequencies. Let

$$\mathbf{x}=\boldsymbol{\Phi}\mathbf{q}, \tag{19}$$

where $\Phi=[\varphi^{(1)},\varphi^{(2)},\ldots,\varphi^{(n)}]$ is the main modal matrix; $\mathbf{q}=\{q_1,q_2,\ldots,q_n\}^T$. Substituting equation (19) into equation (16) and multiplying $\boldsymbol{\Phi}^{\mathrm{T}}$ by left, the regular modal equation can be obtained as

$$\boldsymbol{\Phi}^T\mathbf{M}\boldsymbol{\Phi}\ddot{\mathbf{q}}+\boldsymbol{\Phi}^T(\mathbf{K}_a+\mathbf{K}_v)\boldsymbol{\Phi}\mathbf{q}=\mathbf{0}. \tag{20}$$

Expansions of equation (20) are

$$\begin{aligned}&\ddot{q}_n+\omega_n^2q_n+2\sum_{r=1}^{L}\sum_{l=1}^{\infty}\Big[\varepsilon_{s1a}\left(A_{nr}^{(l)}\cos l\omega_{s1a}t+B_{nr}^{(l)}\sin l\omega_{s1a}t\right)+\varepsilon_{r1b}\left(C_{nr}^{(l)}\cos l\omega_{r1b}t+D_{nr}^{(l)}\sin l\omega_{r1b}t\right)\\ &+\varepsilon_{s2p}\left(E_{nr}^{(l)}\cos l\omega_{s2p}t+F_{nr}^{(l)}\sin l\omega_{s2p}t\right)+\varepsilon_{r2p}\left(G_{nr}^{(l)}\cos l\omega_{r2p}t+H_{nr}^{(l)}\sin l\omega_{r2p}t\right)q_r\Big]=0,\quad n=1,2,\ldots,L,\end{aligned} \tag{21}$$

where $L = 5+2M+N$ and $\varepsilon_m = k_m^v/k_m^a$. The expressions of coefficient terms $A_{nr}^{(l)}$, $B_{nr}^{(l)}$, $C_{nr}^{(l)}$, $D_{nr}^{(l)}$, $E_{nr}^{(l)}$, $F_{nr}^{(l)}$, $G_{nr}^{(l)}$, and $H_{nr}^{(l)}$ are shown in Appendix B.

Using multiscale method, time variables representing different scales are introduced:

$$\begin{aligned} T_0 &= t, \\ T_1 &= \varepsilon t. \end{aligned} \tag{22}$$

The solution of equation (21) is expressed as

$$q_n(t,\varepsilon) = q_{n0}(T_0, T_1) + \varepsilon q_{n1}(T_0, T_1), \quad n = 1, 2, \ldots, L. \tag{23}$$

Substituting equation (23) into equation (21), collecting terms of the same power in ε on both sides of the equation yields

$$q_{n0} = A_n(T_1)e^{i\omega_n T_0} + cc, \tag{24}$$

$$\begin{aligned} D_0^2 q_{n1} + \omega_n^2 q_{n1} = {} & -2i\omega_n e^{i\omega_n t} D_1 A_n \\ & - 2\sum_{r=1}^{L}\sum_{l=1}^{\infty}\Big[\frac{\varepsilon_{s1a}}{\varepsilon}\left(A_{nr}^{(l)}\cos l\omega_{s1a}t + B_{nr}^{(l)}\sin l\omega_{s1a}t\right) + \frac{\varepsilon_{r1b}}{\varepsilon}\left(C_{nr}^{(l)}\cos l\omega_{r1b}t + D_{nr}^{(l)}\sin l\omega_{r1b}t\right) \\ & + \frac{\varepsilon_{s2p}}{\varepsilon}\left(E_{nr}^{(l)}\cos l\omega_{s2p}t + F_{nr}^{(l)}\sin l\omega_{s2p}t\right) + \frac{\varepsilon_{r2p}}{\varepsilon}\left(G_{nr}^{(l)}\cos l\omega_{r2p}t + H_{nr}^{(l)}\sin l\omega_{r2p}t\right)\Big]q_{r0}, \end{aligned} \tag{25}$$

where A_n (T_1) is the amplitude in complex form, $\varepsilon = \max\{\varepsilon_{s1a}, \varepsilon_{r1b}, \varepsilon_{s2p}, \varepsilon_{r2p}\}$, and cc is the complex conjugate of preceding items. Substitution of equation (24) into equation (25) yields

$$\begin{aligned} D_0^2 q_{n1} + \omega_n^2 q_{n1} = {} & -2i\omega_n e^{i\omega_n t} D_1 A_n - \sum_{r=1}^{L}\sum_{l=1}^{\infty}\Big[\frac{\varepsilon_{s1a}}{\varepsilon}\left(A_{nr}^{(l)} + iB_{nr}^{(l)}\right)\left(A_r e^{i(\omega_r + l\omega_{s1a})t} + \overline{A}_r e^{i(-\omega_r + l\omega_{s1a})t}\right) \\ & + \frac{\varepsilon_{r1b}}{\varepsilon}\left(C_{nr}^{(l)} + iD_{nr}^{(l)}\right)\left(A_r e^{i(\omega_r + l\omega_{r1b})t} + \overline{A}_r e^{i(-\omega_r + l\omega_{r1b})t}\right) \\ & + \frac{\varepsilon_{s2p}}{\varepsilon}\left(E_{nr}^{(l)} + iF_{nr}^{(l)}\right)\left(A_r e^{i(\omega_r + l\omega_{s2p})t} + \overline{A}_r e^{i(-\omega_r + l\omega_{s2p})t}\right) \\ & + \frac{\varepsilon_{r2p}}{\varepsilon}\left(G_{nr}^{(l)} + iH_{nr}^{(l)}\right)\left(A_r e^{i(\omega_r + l\omega_{r2p})t} + \overline{A}_r e^{i(-\omega_r + l\omega_{r2p})t}\right) + cc. \end{aligned} \tag{26}$$

It can be seen from the above that, in addition to the fact that the meshing frequency is close to the natural frequency of the system to excite the main resonance, when the frequency $l\omega_m$ is close to the natural frequency combination $\omega_n \pm \omega_r$, there will be a secular term in the equation and an unstable region of parameter vibration in the gear system.

5. Meshing Stiffness Parametric Vibration

The parameters of the coaxial contrarotating encased differential gear train are shown in Table 1. The meshing frequency of each gear pair of the system is [15]

$$\begin{aligned} f_{s1ai} &= \frac{n_{\text{in}} z_{s1}}{60}, \\ f_{r1bi} &= \frac{n_{\text{in}} z_{s1} z_b}{60 z_a}, \\ f_{s2pj} &= \frac{2 n_{\text{in}} z_{r2} z_{s1} z_b}{60 z_{r1} z_a}, \\ f_{r2pj} &= \frac{2 n_{\text{in}} z_{r2} z_{s1} z_b}{60 z_{r1} z_a}, \end{aligned} \tag{27}$$

where n_{in} is the input speed (r/min).

Table 1: Encased differential gear train parameters.

Parameter	Parameter values
Number of planets	$M = N = 3$
Number of teeth	$z_{s1} = 57$, $z_a = 54$, $z_b = 18$, $z_{r1} = 107 z_{s2} = 38$, $z_p = 25$, $z_{r2} = 88$
Modulus (mm)	$m_{s1} = 2.75$, $m_{r1} = 3.5$, $m_{s2} = 4$, $m_{r2} = 4$
Pressure angle (°)	$\alpha_{s1} = 20$, $\alpha_a = 20$, $\alpha_b = 20$, $\alpha_{r1} = 20\, \alpha_{s2} = 20$, $\alpha_{r2} = 20$, $\alpha_p = 20$
Planet mass (kg)	$m_p = 2.156$
Moment of inertia ($\mathrm{kg \cdot m^2}$)	$I_{s1} = 0.0423$, $I_a = 0.011$, $I_b = 0.00076$, $I_{r1} = 1.1475 I_{s2} = 0.0223$, $I_p = 0.0037$, $I_{r2} = 2.059$, $I_{c2} = 0.3413$
Base radius (mm)	$r_{bs1} = 73.62$, $r_{ba} = 69.77$, $r_{bb} = 29.6$, $r_{br1} = 175.96$, $r_{bs2} = 71.42$, $r_{bp} = 46.98$, $r_{br2} = 165.39$, $r_{c2} = 126$
Mesh stiffness k_m^a (N/m)	$k_{s1ai}^a = 4.20 \times 10^8$, $k_{r1bi}^a = 3.70 \times 10^8$, $k_{s2pj}^a = 3.53 \times 10^8$, $k_{r2pj}^a = 3.93 \times 10^8$
Mesh stiffness k_m^v (N/m)	$k_{s1ai}^v = 0.81 \times 10^8$, $k_{r1bi}^v = 0.73 \times 10^8$, $k_{s2pj}^v = 0.66 \times 10^8$, $k_{r2pj}^v = 0.71 \times 10^8$
Torsional stiffness (N·m/rad)	$k_s = 2.4 \times 10^6$, $k_x = 8.6 \times 10^5$, $k_r = 5.7 \times 10^8$
Damping coefficient	$\xi_m = 0.07$, $\xi_z = 0.075$
Working pressure angles (°)	$\alpha'_{s2p} = 20$, $\alpha'_{r2p} = 20$
Mesh phasing	$\gamma_{s1ai} = [0, 0, 0]$, $\gamma_{r1bi} = [0.1246, 0.4579, 0.7913]$, $\gamma_{s2pj} = [0.1978, 0.8645, 0.5311]$, $\gamma_{r2pj} = [0.0432, 0.7099, 0.3765]$

Table 2: Natural frequencies for the system (Hz).

Order	1	2	3	4	5	6	7	8	9	10	11	12	13	14
Frequency	0	473	1167	2246	2246	2300	3117	3356	3356	4015	4490	6413	6413	6439

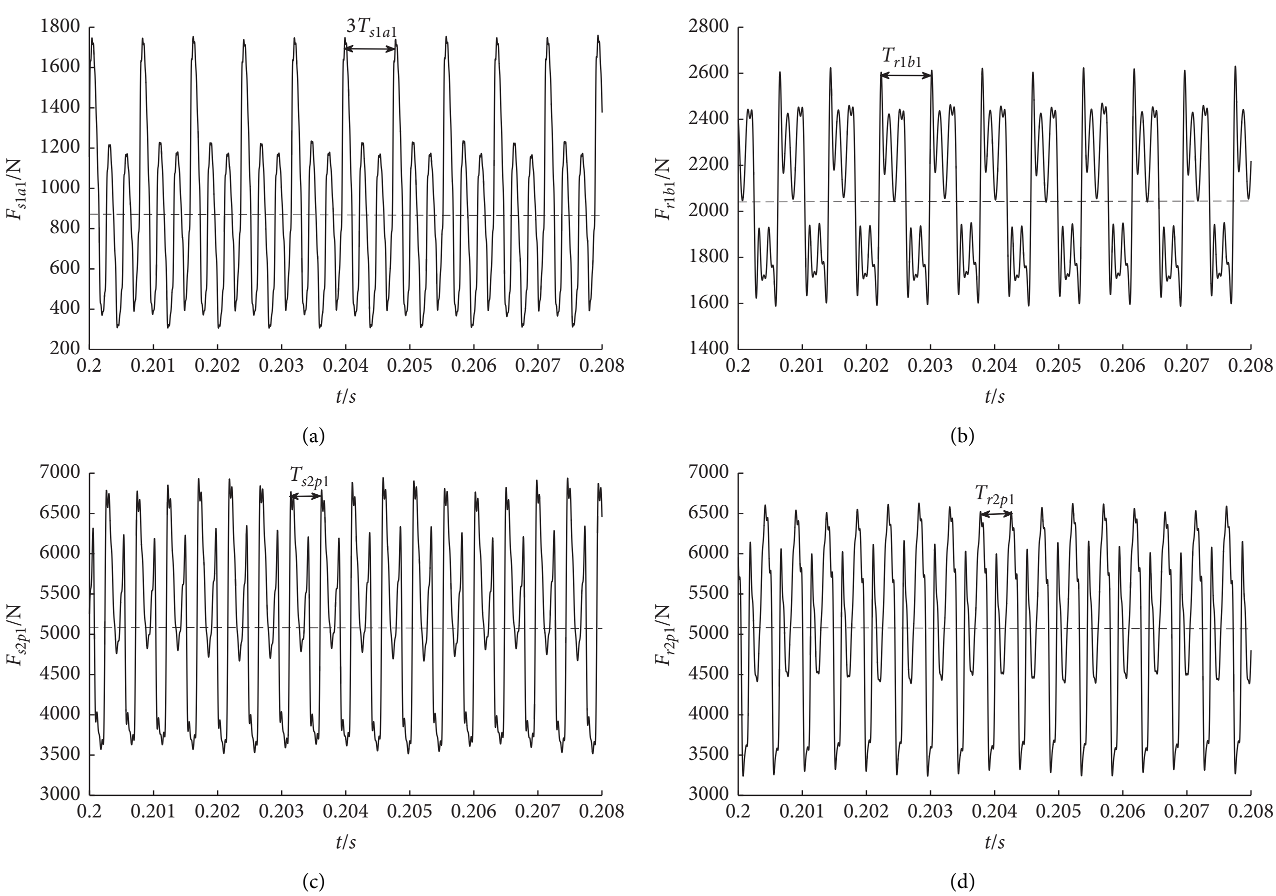

Figure 3: Dynamic meshing force of gear pair.

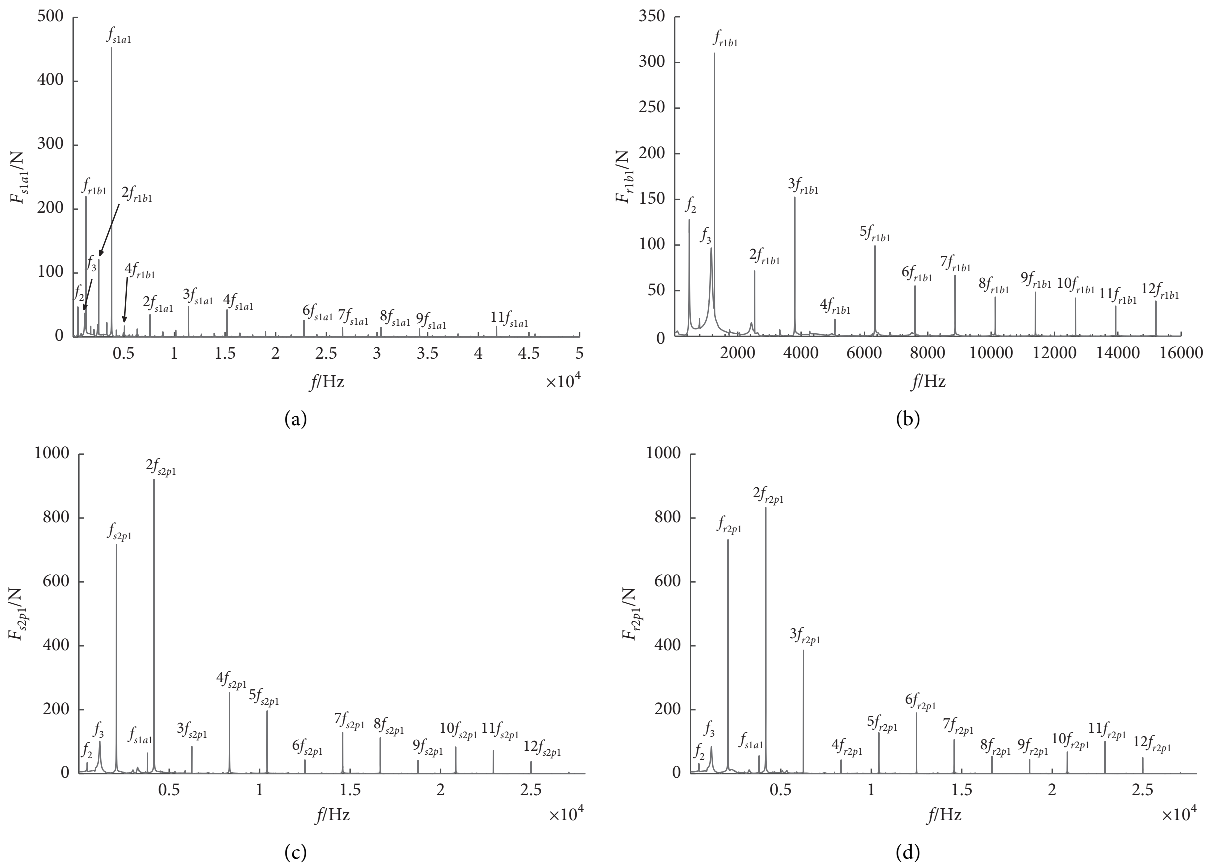

Figure 4: Spectrum of meshing forces ($n_{s1} = 4000$ r/min).

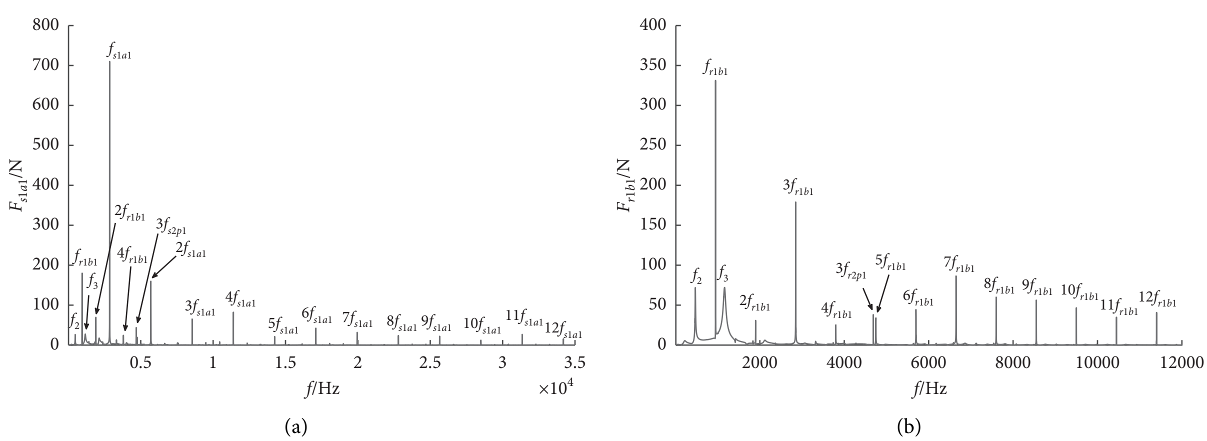

Figure 5: Continued.

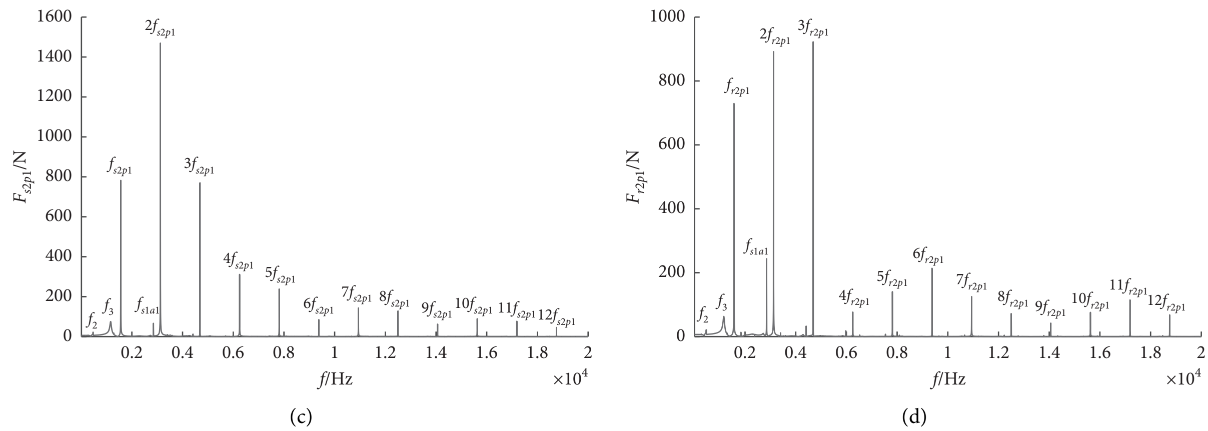

FIGURE 5: Spectrum of meshing forces ($n_{s1} = 3000$ r/min).

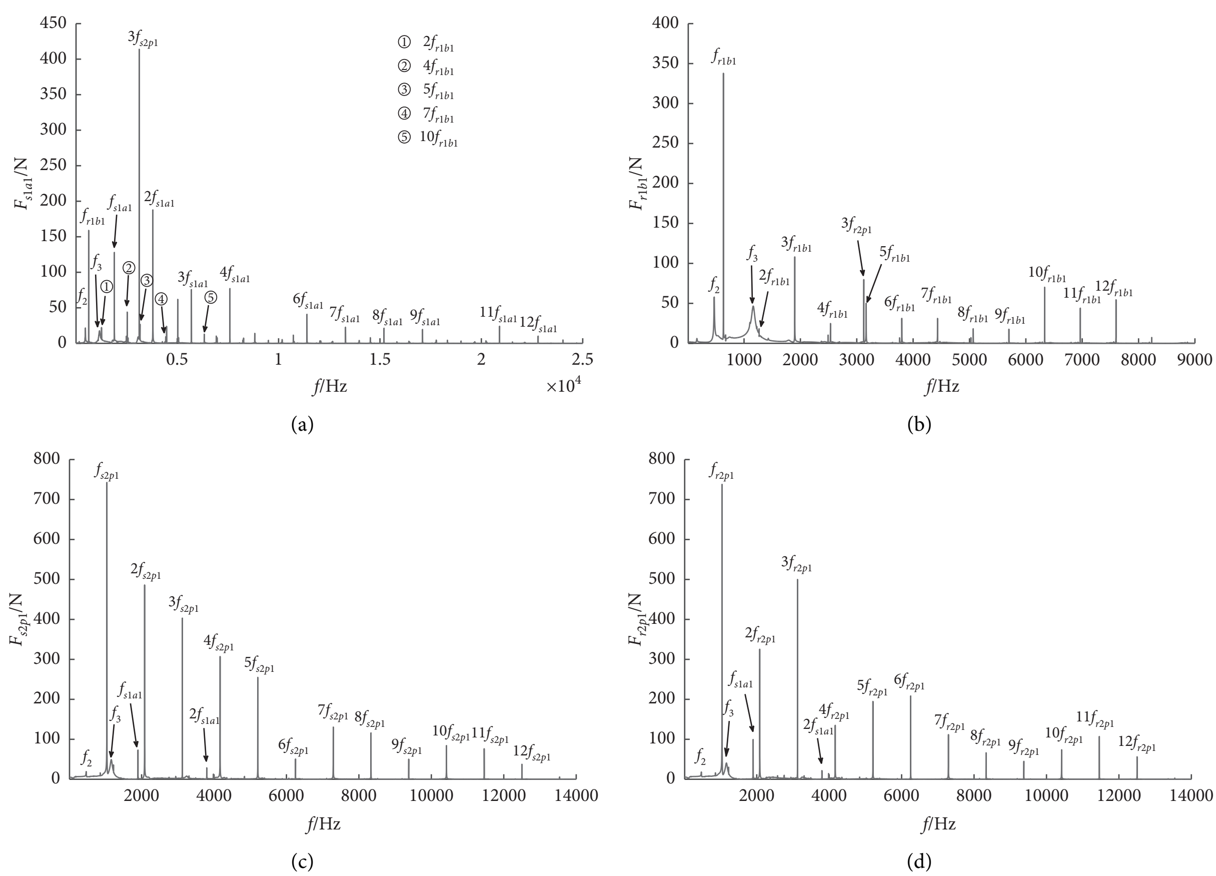

FIGURE 6: Spectrum of meshing forces ($n_{s1} = 2000$ r/min).

5.1. Natural Frequency. Natural frequencies of the encased differential gear train are obtained from equation (17), as shown in Table 2. It can be divided into three types according to its multiplicity: eight natural frequencies always have multiplicity 1, two groups of M–1 multiples (f_4/f_5, f_{12}/f_{13}), and one group of N-1 multiples (f_8/f_9), which, respectively, correspond to the torsional vibration mode, stepped planet mode, and planet mode of the system. Frequency of 0 represents the rigid body motion of the system, and the magnitude of multiple frequencies is independent of the number of planets [17].

5.2. Dynamic Characteristics of Elastic Meshing Force. The elastic meshing force of gear pair m in the encased differential gear train is expressed as $F_m(t) = k_m(t)\,\delta_m$. It is defined that input torque $T_{in} = 1283.5\,\text{N·m}$ is constant, and the

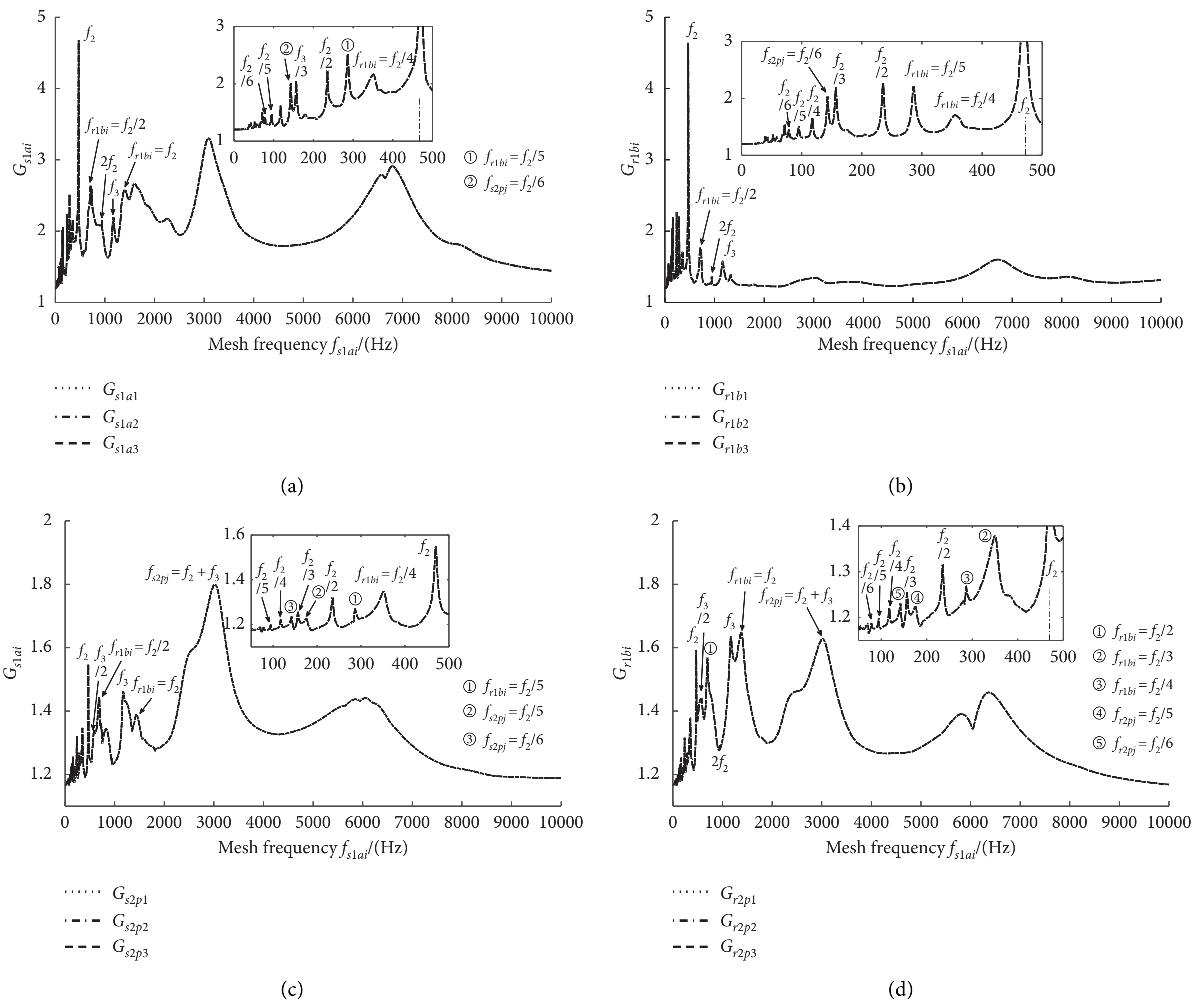

Figure 7: Dynamic load factors of the encased differential gear train.

output torque $T_{ou1} = T_{ou2} = iT_{in}/2$, where i is the gear system transmission ratio. The Runge-Kutta method is used to solve the numerical solution of the differential equations.

5.2.1. Time-Domain Analysis of Meshing Force. When the torque is constant and the input speed is $ns1 = 4000$ r/min, the meshing force of gear pairs is shown in Figure 3. It can be seen from the figure that the dynamic meshing force fluctuates around the static meshing force value shown by the dotted line. The meshing force F_{s1a1} fluctuates with its own meshing period. The meshing forces F_{r1b1}, F_{s2p1}, and F_{r2p1} mainly fluctuate in their own periods, and they also have high-frequency fluctuations of small amplitude. This is caused by the excitation of the time-varying stiffness parameters such as mesh phasing and contact ratio.

5.2.2. Frequency-Domain Analysis of Meshing Force. The frequency spectrum of system meshing force at different input speeds and constant torque is shown in Figures 4–6. It can be seen from the figures that, in addition to the meshing frequency of its own planetary set, the meshing frequency of other planetary sets and natural frequencies f_2 and f_3 also appear in the meshing force, which indicates that the system has multifrequency coupling vibration.

As shown in Figure 4, when the input speed is $n_{in} = 4000$ r/min, the meshing frequency f_{r1b1} appears in the frequency spectrum of the meshing force F_{s1a1} of the encased stage, and the encased stage meshing frequency f_{s1a1} appears in the spectrum of differential stage meshing forces F_{s2p1} and F_{r2p1}, but there is no differential stage meshing frequency in the encased stage meshing force spectrum, which indicates that the meshing frequency coupling relationship between the meshing forces of different planetary sets is not equal. As shown in Figures 5 and 6, when the rotating speed is $n_{in} = 3000$ r/min and $n_{in} = 2000$ r/min, in addition to the above coupling effect, there is also coupling of differential stage meshing frequency in the encased stage meshing force spectrum.

This is because the torsional internal force of the connecting shaft couples the vibration displacements of different frequencies together and then acts on the two connected parts in the form of acting force and reaction force, respectively. The connected coupling parts will return back the vibration displacement with new frequency to the meshing force of the planetary set in the form of equivalent meshing line deformation, resulting in the intercoupling between the meshing forces of different planetary sets [18].

5.3. Analysis of the Dynamic Load Characteristics. In the compound planetary gear transmission, different meshing states will cause difference between the multiple external and internal meshing forces of the same planetary set and will also form the different dynamic characteristics of the meshing forces of each planetary set. In this paper, the dynamic load factor is used to evaluate the dynamic characteristics of meshing forces.

The dynamic load factor G_m is the ratio of the maximum dynamic load to the static load on the gear teeth during a meshing period; that is [19],

$$G_m = \max \frac{\{F_m(t)\}}{F_m'}, \tag{28}$$

where F_m' is the static meshing force.

It can be seen from Figure 7 that, in the range of the speed variation, the dynamic load factor of the gear pair $s1ai$ is significantly larger than that of other meshing pairs, which is because the gear pair $s1ai$ is a high-speed gear train and its vibration is relatively severe. The load distribution among the planets in each planetary set of the system is very uniform.

According to Figures 7(a) and 7(b), the system has a strong main resonance response when the meshing frequency f_{s1ai} is close to the natural frequency f_2, and the dynamic load factors G_{s1ai} and G_{r1bi} of the encased stage gear pair are very large. Due to the time-varying meshing stiffness, the meshing frequency f_{s1ai} causes the superharmonic responses and 1/2 subharmonic response of the encased stage, and the meshing frequencies f_{r1bi} and f_{s2pj} also cause the superharmonic responses.

From Figures 7(c) and 7(d), in addition to the main resonance response, superharmonic response, and subharmonic response, the dynamic load factor of the differential stage also peaks at $f_{s2pj} = f_2 + f_3$, corresponding to the combined resonance of the additive type.

6. Conclusions

In this paper, the torsional dynamic characteristics of the coaxial contrarotating encased differential gear system are studied, and the natural frequency of the system is obtained. The time-domain and frequency-domain characteristics of the elastic meshing force are analyzed, and the variation of dynamic load factor with the input rotating speed is studied.

(1) Natural frequencies of the encased differential gear train can be divided into 3 types according to its multiplicity, which correspond to the torsional vibration mode, stepped planet mode, and planet mode.

(2) The dynamic meshing force fluctuates around the static meshing force value. The meshing force of the gear pair $s1a1$ fluctuates with its own meshing period. The meshing forces of gear pairs $s1b1$, $s2p1$, and $r2p1$ fluctuate mainly in their own periods, and they also have high-frequency fluctuations of small amplitude.

(3) In addition to the meshing frequency of its own planetary set, the meshing force spectrum also includes the meshing frequency of other planetary sets and the natural frequency of the system.

(4) The dynamic load factor of the gear pair $s1ai$ is significantly larger than those of the other meshing pairs. The dynamic load factor of the gear pair of the system peaks not only at the main resonance response but also at the superharmonic response, subharmonic response, and combined resonance response.

Appendix

A. Expression of Dynamic Parameter Matrix

$$\mathbf{M} = \operatorname{diag}\left[\frac{I_{s1}}{r_{bs1}^2}, \frac{I_{s2}}{r_{bs2}^2}, \frac{I_{r1}}{r_{br1}^2}, \frac{I_{r2}}{r_{br2}^2}, \frac{I_{c2}+NI_p}{r_{c2}^2} + Nm_p, \frac{I_{a1}}{r_{ba}^2}, \ldots, \frac{I_{aM}}{r_{ba}^2}, \frac{I_{b1}}{r_{bb}^2}, \ldots, \frac{I_{bM}}{r_{bb}^2}, \frac{I_{pj}}{r_{bp}^2}, \ldots, \frac{I_{pj}}{r_{bp}^2}\right],$$

$$\mathbf{Q} = \left[\frac{T_{\text{in}}}{r_{bs1}} \;\; 0 \;\; 0 \;\; -\frac{T_{ou1}}{r_{br2}} \;\; -\frac{T_{ou2}}{r_{c2}} \;\; \overbrace{0 \;\ldots\; 0}^{M} \;\; \overbrace{0 \;\ldots\; 0}^{M} \;\; \overbrace{0 \;\ldots\; 0}^{N}\right]^T,$$

$$\mathbf{K} = [\,\mathbf{K}_1 \;\; \mathbf{K}_2\,],$$

$$\mathbf{K}_1 = \begin{bmatrix}
\sum_{i=1}^{M} k_{s1ai} + \frac{k_s}{r_{bs1}^2} & -\frac{k_s}{r_{bs1} r_{bs2}} & 0 & 0 & 0 \\
-\frac{k_s}{r_{bs1} r_{bs2}} & \sum_{j=1}^{N} k_{s2pj} + \frac{k_s}{r_{bs2}^2} & 0 & 0 & -\sum_{j=1}^{N} k_{s2pj} \cos\alpha'_{s2p} \\
0 & 0 & \sum_{i=1}^{M} k_{r1bi} + \frac{k_r}{r_{br1}^2} & -\frac{k_r}{r_{br1} r_{br2}} & 0 \\
0 & 0 & -\frac{k_r}{r_{br1} r_{br2}} & \frac{k_r}{r_{br2}^2} + \sum_{j=1}^{N} k_{r2pj} & \sum_{j=1}^{N} k_{s2pj} \cos\alpha'_{r2p} \\
0 & -\sum_{j=1}^{N} k_{s2pj} \cos\alpha'_{s2p} & 0 & \sum_{j=1}^{N} k_{r2pj} \cos\alpha'_{r2p} & \sum_{j=1}^{N} \left(k_{s2pj} \cos\alpha'_{s2p} + k_{r2pj} \cos\alpha'_{r2p}\right) \\
-k_{s1a1} & 0 & 0 & 0 & 0 \\
\ldots & 0 & 0 & 0 & 0 \\
-k_{s1aM} & 0 & 0 & 0 & 0 \\
0 & 0 & -k_{r1b1} & 0 & 0 \\
0 & 0 & \ldots & 0 & 0 \\
0 & 0 & -k_{r1bM} & 0 & 0 \\
0 & -k_{s2p1} & 0 & -k_{r2p1} & k_{s2p1} \cos\alpha'_{s2p} - k_{r2p1} \cos\alpha'_{r2p} \\
0 & \ldots & 0 & \ldots & \ldots \\
0 & -k_{s2pN} & 0 & -k_{r2pN} & k_{s2pN} \cos\alpha'_{s2p} - k_{r2pN} \cos\alpha'_{r2p}
\end{bmatrix},$$

$$\mathrm{K}_2 = \begin{bmatrix}
-k_{s1a1} & \cdots & -k_{s1aM} & 0 & 0 & 0 & 0 & 0 & 0 \\
0 & 0 & 0 & 0 & 0 & 0 & -k_{s2p1} & \cdots & -k_{s2pN} \\
0 & 0 & 0 & -k_{r1b1} & \cdots & -k_{r1bM} & 0 & 0 & 0 \\
0 & 0 & 0 & 0 & 0 & 0 & -k_{r2p1} & \cdots & -k_{r2pN} \\
0 & 0 & 0 & 0 & 0 & 0 & k_{s2p1}\cos\alpha'_{s2p} - k_{r2p1}\cos\alpha'_{r2p} & \cdots & k_{s2pN}\cos\alpha'_{s2p} - k_{r2pN}\cos\alpha'_{r2p} \\
k_{s1a1} + \dfrac{k_x}{r_{ba}^2} & 0 & 0 & -\dfrac{k_x}{r_{ba}r_{bb}} & 0 & 0 & 0 & 0 & 0 \\
0 & \ddots & 0 & 0 & 0 & 0 & 0 & 0 & 0 \\
0 & 0 & k_{s1aM} + \dfrac{k_x}{r_{ba}^2} & 0 & 0 & -\dfrac{k_x}{r_{ba}r_{bb}} & 0 & 0 & 0 \\
-\dfrac{k_x}{r_{bb}r_{ba}} & 0 & 0 & \dfrac{k_x}{r_{bb}^2} + k_{r1b1} & 0 & 0 & 0 & 0 & 0 \\
0 & 0 & 0 & 0 & \ddots & 0 & 0 & 0 & 0 \\
0 & 0 & -\dfrac{k_x}{r_{bb}r_{ba}} & 0 & 0 & \dfrac{k_x}{r_{bb}^2} + k_{r1bM} & 0 & 0 & 0 \\
0 & 0 & 0 & 0 & 0 & 0 & k_{s2p1} + k_{r2p1} & 0 & 0 \\
0 & 0 & 0 & 0 & 0 & 0 & 0 & \ddots & 0 \\
0 & 0 & 0 & 0 & 0 & 0 & 0 & 0 & k_{s2pN} + k_{r2pN}
\end{bmatrix}. \tag{A.1}$$

B. Expression of Coefficient Term

$$\begin{aligned}
A_{nr}^{(l)} &= \sum_{i=1}^{M} k_{s1ai}^{a} a_{s1ai}^{(l)} \delta_{s1ai}^{(n)} \delta_{s1ai}^{(r)}, \\
B_{nr}^{(l)} &= \sum_{i=1}^{M} k_{s1ai}^{a} b_{s1ai}^{(l)} \delta_{s1ai}^{(n)} \delta_{s1ai}^{(r)}, \\
C_{nr}^{(l)} &= \sum_{i=1}^{M} k_{r1bi}^{a} a_{r1bi}^{(l)} \delta_{r1bi}^{(n)} \delta_{r1bi}^{(r)}, \\
D_{nr}^{(l)} &= \sum_{i=1}^{M} k_{r1bi}^{a} b_{r1bi}^{(l)} \delta_{r1bi}^{(n)} \delta_{r1bi}^{(r)}, \\
E_{nr}^{(l)} &= \sum_{j=1}^{N} k_{s2pj}^{a} a_{s2pj}^{(l)} \delta_{s2pj}^{(n)} \delta_{s2pj}^{(r)}, \\
F_{nr}^{(l)} &= \sum_{j=1}^{N} k_{s2pj}^{a} b_{s2pj}^{(l)} \delta_{s2pj}^{(n)} \delta_{s2pj}^{(r)}, \\
G_{nr}^{(l)} &= \sum_{j=1}^{N} k_{r2pj}^{a} a_{r2pj}^{(l)} \delta_{r2pj}^{(n)} \delta_{r2pj}^{(r)}, \\
H_{nr}^{(l)} &= \sum_{j=1}^{N} k_{r2pj}^{a} b_{r2pj}^{(l)} \delta_{r2pj}^{(n)} \delta_{r2pj}^{(r)}.
\end{aligned} \tag{B.1}$$

Data Availability

The data used to support the findings of this study are available from the corresponding author upon request.

Conflicts of Interest

The authors declare that there are no conflicts of interest regarding the publication of this paper.

Acknowledgments

This work was supported by the National Key R&D Program of China (Grant no. 2018YFB2001300).

References

[1] D. C. Howe and A. H. Mckibbin, “Design of a gear drive system for counter-rotating fan rotors,” in *Proceedings of the 25th Joint Propulsion Conference*, pp. 1–11, Monterey, CA, USA, July 1989.

[2] D. C. Howe, C. V. Sundt, and A. H. Mckibbon, “Advanced counter-rotating gearbox detailed design report,” NASA, Washington, NJ, USA, CR-180883, 1988.

[3] J. Lin and R. G. Parker, “Mesh stiffness variation instabilities in two-stage gear systems,” *Journal of Vibration and Acoustics*, vol. 124, no. 1, pp. 68–76, 2002.

[4] J. Lin and R. G. Parker, "Planetary gear parametric instability caused by mesh stiffness variation," *Journal of Sound and Vibration*, vol. 249, no. 1, pp. 129–145, 2002.

[5] G. Liu, J. Hong, and R. G. Parker, "Influence of simultaneous time-varying bearing and tooth mesh stiffness fluctuations on spur gear pair vibration," *Nonlinear Dynamics*, vol. 97, no. 2, pp. 1403–1424, 2019.

[6] X. H. Qiu, Q. Han, and F. L. Chu, "Investigation of parametric instability of the planetary gear under speed fluctuations," *Shock and Vibration*, vol. 2017, Article ID 6851903, 14 pages, 2017.

[7] X. H. Qiu, Q. K Han, and F. L. Chu, "Parametric instability in planetary gears with frequency modulated time-varying mesh stiffness," in *Proceedings of the ASME 2014 International Design Engineering Technical Conferences & Computers and Information in Engineering Conference*, New York, NY, USA, August 2014.

[8] S. V. Canchi and R. G. Parker, "Effect of ring-planet mesh phasing and contact ratio on the parametric instabilities of a planetary gear ring," *Journal of Mechanical Design*, vol. 130, p. 14501, 2008.

[9] R. G. Parker, "Vibration of planetary gears with elastically deformable ring gears parametrically excited by mesh stiffness fluctuations," in *Proceedings of the ASME 2009 International Design Engineering Technical Conferences & Computers and Information in Engineering Conference*, San Diego, California, USA, January 2009.

[10] R. G. Parker and X. Wu, "Parametric instability of planetary gears having elastic continuum ring gears," *Journal of Vibration and Acoustics*, vol. 134, no. 4, p. 41011, 2012.

[11] M. Inalpolat and A. Kahraman, "A dynamic model to predict modulation sidebands of a planetary gear set having manufacturing errors," *Journal of Sound and Vibration*, vol. 329, no. 4, pp. 371–393, 2010.

[12] P. Sondkar and A. Kahraman, "A dynamic model of a double-helical planetary gear set," *Mechanism and Machine Theory*, vol. 70, pp. 157–174, 2013.

[13] W. Sun, X. Li, J. Wei, A. Zhang, X. Ding, and X. Hu, "A study on load-sharing structure of multi-stage planetary transmission system," *Journal of Mechanical Science and Technology*, vol. 29, no. 4, pp. 1501–1511, 2015.

[14] H. Dong, Y. Wu, D. Wang, and S. Bai, "M-DOF dynamic model for load sharing behavior analysis of PGT," *Journal of Mechanical Science and Technology*, vol. 30, no. 3, pp. 993–1001, 2016.

[15] D. L. Zhang, R. P. Zhu, B. B. Fu et al., "Mesh phase analysis of encased differential gear train for coaxial twin-rotor helicopter," *Mathematical Problems in Engineering*, vol. 2019, Article ID 8421201, 9 pages, 2019.

[16] V. K. Tamminana, A. Kahraman, and S. Vijayakar, "A study of the relationship between the dynamic factor and the dynamic transmission error of spur gear pairs," in *Proceedings of the ASME 2009 International Design Engineering Technical Conferences &Computers and Information in Engineering Conference*, San Diego, CA, USA, August 2005.

[17] J. Lin and R. G. Parker, "Analytical characterization of the unique properties of planetary gear free vibration," *Journal of Vibration and Acoustics*, vol. 121, no. 3, pp. 316–321, 1999.

[18] H. Liu, Z. C. Cai, and C. L. Xiang, "Frequency coupling and dynamic characteristics of nonlinear meshing force for two-stage planetary gears," *Journal of Vibration and Shock*, vol. 34, no. 19, pp. 13–23, 2015, in Chinese.

[19] Z. Sun, Y. W. Shen, and S. Y. Li, "Study on dynamic behavior of encased differential gear train," *Chinese Journal of Mechanical Engineering*, vol. 38, no. 02, pp. 44–52, 2002, in Chinese.